Research Article / Mechanical and Materials Engineering https://doi.org/10.15446/ing.investig.v41n1.85825

Accelerated Adaptive Backstepping Control of the Chaotic MEMS Gyroscope by Using the Type-2 Sequential FNN

Control acelerado del backstepping adaptativo del giroscopio caótico MEMS por medio de la FNN secuencial de tipo 2

Le Zhao[1], Shaohua Luo[2], Guanci Yang[3], and Junyang Li[4]

ABSTRACT

In this paper, we propose an accelerated adaptive backstepping control algorithm based on the type-2 sequential fuzzy neural network (T2SFNN) for the micro-electromechanical system (MEMS) gyroscope with dead-zone and constraints. Firstly, the mathematical model of the MEMS gyroscope is established to perform dynamical analyses and controller design. Then, the phase diagrams and Lyapunov exponents are presented to reveal its chaotic oscillation, which is harmful to system stability. In order to suppress oscillations derived from chaos and dead-zone, an accelerated adaptive backstepping controller is proposed wherein an adaptive auxiliary is established to compensate the influence of nonsymmetric dead-zone on stability performance, along with the T2SFNN designed to approximate unknown functions of dynamic systems. Furthermore, the speed function is introduced to accelerate convergence speed of the control system, and the problem of complex term explosion in traditional backstepping is successfully solved by a second-order tracking differentiator. Finally, simulation results show that the proposed control scheme can guarantee asymptotic convergence of all signals in the closed-loop system, as well as satisfying states constraints and fulfilling the purposes of chaos suppression and accelerated convergence.

Keywords: MEMS gyroscope, type-2 sequential fuzzy neural network, accelerated backstepping control, chaotic oscillation, speed function

RESUMEN

En este artículo se propone un algoritmo de control acelerado y autoadaptado de backstepping basado en la red neural analgésica de tipo 2 (T2SFNN) para giroscopios del sistema microeléctrico (MEMS) con zona muerta y limitaciones. En primer lugar, se establece el modelo matemático del giroscopio MEMS para realizar análisis dinámicos y diseño de controladores. Luego, se presentan los diagramas de fase y los exponentes de Lyapunov para revelar su oscilación caótica, que es perjudicial para la estabilidad del sistema. Con el fin de suprimir las oscilaciones derivadas del caos y la zona muerta, se propone un controlador de backstepping adaptativo acelerado en el que se establece un auxiliar adaptativo para compensar la influencia de la zona muerta no simétrica en el rendimiento de estabilidad, junto con el T2SFNN diseñado para aproximar funciones desconocidas de sistema dinámico. Además, se introduce la función de velocidad para acelerar la velocidad de convergencia del sistema de control, y el problema de la explosión de términos complejos en el backstepping tradicional es resuelto exitosamente por un diferenciador de seguimiento de segundo orden. Finalmente, los resultados de la simulación muestran que el esquema de control propuesto puede garantizar la convergencia asintótica de todas las señales en el sistema de circuito cerrado, además de satisfacer las restricciones de los estados y lograr los propósitos de supresión del caos y convergencia acelerada.

Palabras clave: giroscopio MEMS, red neuronal difusa secuencial de tipo 2, control acelerado de backstepping, oscilación caótica, función de velocidad

Received: March 22nd, 2020
Accepted: October 27th, 2020

Introduction

In view of the advantages of measuring the angular velocity of objects, low energy consumption, high integration, and simple structure, the MEMS gyroscope is widely used in vehicle navigation and positioning system, control, aerospace, the social robot, and other fields (Lin, Li, and Yang, 2020; Chong *et al.*, 2016; Fang, Fei, and Yang, 2018; Rahmani, 2018; Rahmani and Rahman, 2018; Su, Li, and Yang, 2020). Unfortunately, due to the influence of manufacturing errors and working environment changes, the measuring accuracy of the MEMS gyroscope will be greatly reduced. On top of that, the inherent characteristics of MEMS gyroscopes,

[1]School of Mechanical Engineering, Guizhou University, China. Affiliation: Student. Email: lezhao0813@126.com
[2]School of Mechanical Engineering, Key Laboratory of Advanced Manufacturing Technology, Guizhou University, China. Ph.D. Affiliation: Full professor. Email: shluo@gzu.edu.cn
[3]Key Laboratory of Advanced Manufacturing Technology, Guizhou University, China. Ph.D. Affiliation: Full professor. Email: gcyang@gzu.edu.cn
[4]State Key Laboratory of Mechanical Transmission, Chongqing University, China. Ph.D. Affiliation: Full professor. Email: junyangli@cqu.edu.cn

How to cite: Le, Z., Shaohua, L., Guanci, Y., and Junyang, L. (2021). Accelerated Adaptive Backstepping Control of the Chaotic MEMS Gyroscope by Using the Type-2 Sequential FNN. *Ingeniería e Investigación*, *41*(1), e85825. 10.15446/ing.investig.v41n1.85825

such as dead-zone hysteresis and chaotic oscillations, will reduce its operational performance, and even cause serious safety accidents. Therefore, it is of profound and lasting significance to design an effective controller to improve the robust performance of the MEMS gyroscope and suppress the chaotic oscillations within it.

With continuous in-depth research, many practical and effective strategies have been proposed, such as adaptive control, backstepping control, sliding mode control, and fuzzy control (Fei and Zhou, 2012; Luo and Song, 2016; Ouakad, Nayfeh, Choura, and Najar, 2015; Xu, Zhang, Li, He, and Shi, 2019). Aiming at a new 3-D chaotic system with an axe-shaped curve of equilibrium points, Vaidyanathan, Sambas, and Mamat (2018)constructed the analog circuits to reveal the dynamic characteristics of this system, and then designed an adaptive synchronization controller to carry out the stable control of this system. For a new five-dimensional four-wing hyperchatic system, they built the analog circuits to reveal motion behavior, and then implemented the synchronisation function via integral sliding mode control (Sambas, Chang, Dolvis, Jacques, and Vaidyanathan, 2019). The integral sliding mode control was designed to synchronize a new 2-scrill chaotic system with four quadratic nonlinear terms, and an analog circuit of the new 2-scroll chaotic system was constructed to check the feasibility of the model (Sambas, Vaidyanathan, Mamat, and Mohamed, 2020). For a three-axis MEMS gyroscope, Fei and Zhou (2012) discussed a robust adaptive control strategy through the coupling of fuzzy and sliding mode controls. In order to address the control problem of the MEMS resonator, Luo and Song (2016) proposed an adaptive backstepping control method based on RBF neural networks with output constraints and uncertain time delays. For the MEMS gyroscope, Xu *et al*. (2019) proposed a non-singular terminal sliding mode control method based on compound neural learning. Ouakad *et al*. (2015) designed a feedback controller to suppress the nonlinear motion of the microbeam resonator, and then used electronic circuits to build the controller to illustrate the feasibility of the design scheme. The control methods mentioned above have some disadvantages, such as slow response speeds, poor robustness and poor anti-interference ability.

The way to improve the robustness and enhance the anti-jamming capability of the MEMS gyroscope is an open issue. Sliding mode control is widely used in nonlinear systems because it shows strong robustness to parameter changes. The fractional sliding mode control method is an effective control method that can effectively suppress external disturbance and improve robustness of the controlled system (Rahmani and Rahman, 2019). For the MEMS gyroscope system, Fei and Chu (2016) proposed a dynamic global proportional integral derivative (PID) sliding mode control method and introduced a dynamic PID sliding surface to reduce chattering. For the robot flexible connecting rod system, Delavari *et al*. designed a fractional sliding mode control method and introduced a particle swarm optimization algorithm to adjust the controller parameters to obtain better control performance (Delavari, Lanusse, and Sabatier, 2013). By comparing with the traditional non-singular sliding mode control, the fractional sliding mode control has better convergence precision. Sun and Ma (2017) presented a tracking fractional sliding mode terminal control method for linear motors. For the grid-connected doubly-fed induction generator system, Xiong, Wang, Mi, and Khan proposed a fractional-order sliding mode control method (2017). The simulation results show that the method can not only guarantee the asymptotical stability of all signals of the closed-loop system, but also has strong anti-interference abilities . The main shortcoming of the proposed fractional order sliding mode control is that the control target crosses the approach equilibrium point back and forth on both sides of sliding mode surface, which leads to chattering, thus affecting the control accuracy and even causing the controller performance to collapse.

In recent years, backstepping control has attracted wide attention due to its recursive and systematic control process (Li and Kang, 2010; T. Sun and Pan, 2019; Tong and Li, 2011). Unfortunately, there is an obvious flaw in traditional backstepping technology; virtual control signal causes "complex item explosions" due to repeated differentiation (Gao *et al.*, 2016; S. Gao, Dong, Ning, Tang, and Li, 2018). In order to address this defect, Pan, Wang, Li, and Yu investigated adaptive command-filtered backstepping control method wherein a command filter is used to eliminate these explosions (2017). Although the command filter can solve this issue, it brings about the issue of controller accuracy degradation. In view of this, a second-order tracking differentiator (Tian, Shen, and Dai, 2014) is introduced into the recursive process of traditional backstepping to solve the problem of "complex term explosions" and ensure the accuracy of the controller.

Motivated by the afore-mentioned research works, we developed an accelerated adaptive backstepping controller for the MEMS gyroscope. The main contributions of the accelerated adaptive backstepping control algorithm are emphasized as follows:

1) In the process of the accelerated adaptive backstepping controller design, the control input can reduce the adverse dead-zone effect in practical engineering applications, and a tracking differentiator is proposed to prevent the complex explosion associated with backstepping.

2) In order to accelerate the convergence speed and ensure that the system reaches a steady state faster, the speed function is integrated in the whole control policy. And the T2SFNN is designed to eliminate the effects of unknown functions and enhance the robustness of the controlled system.

3) Our algorithm not only reduces the chattering of the control input, but also improves the robustness of the system against parameter uncertainty and external interference.

Modeling of the MEMS gyroscope

A conventional MEMS gyroscope is mainly composed of a mass, a cantilever beam, a driving electrode, an induction device, and a base, where the driving electrode applies a driving force to the mass block to cause it to vibrate in the direction of the drive shaft. The displacement and velocity of the mass block in the direction of the detection axis can be measured with the induction device. The schematic diagram of the MEMS gyroscope is depicted in Figure 1.

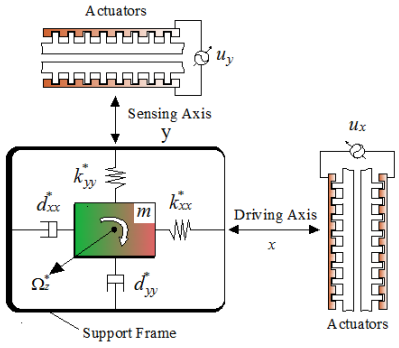

Figure 1. Schematic diagram of the MEMS gyroscope.
Source: Authors

Based on Newtonian mechanics and Kirchhoff's law, the dynamical Equation of the MEMS gyroscope can be expressed as follows (Fang, Yuan, and Fei, 2015; Yan, Hou, Fang, and Fei, 2016):

$$\left.\begin{array}{l} m\ddot{x}+d_{xx}^{*}\dot{x}+d_{xy}^{*}\dot{y}+k_{xx}^{*}x+k_{xy}^{*}y=u_{x}^{*}+d_{x}+2m\Omega_{z}^{*}\dot{y} \\ m\ddot{y}+d_{xy}^{*}\dot{x}+d_{yy}^{*}\dot{y}+k_{xy}^{*}x+k_{yy}^{*}y=u_{y}^{*}+d_{y}-2m\Omega_{z}^{*}\dot{x} \end{array}\right\} \quad (1)$$

where m represents the mass; k_{xy}^*, d_{xy}^* are damping and coupling coefficients; Ω_z^* is the angular velocity along the z-axes; d_{xx}^* and d_{yy}^* are the damping coefficients in the x-y axis direction; k_{xx}^* and k_{yy}^* represent the spring constant in the x-y axis direction; u_x^* and u_y^* are control inputs in x-y axis direction; and d_x and d_y indicate unknown disturbance in x-y axis direction, respectively.

Let$x_1 = x$, $x_2 = \dot{x}$, $x_3 = y$ and $x_4 = \dot{y}$, the dimensionless Equation governing the MEMS gyroscope is rewritten as follows:

$$\begin{array}{l} \dot{x}_1=x_2 \\ \dot{x}_2=-d_{xx}x_2-d_{xy}x_4-\omega_x^2x_1-\omega_{xy}x_3+2\Omega_zx_4 \\ \qquad +d_x+D\left(u_x\right) \\ \dot{x}_3=x_4 \\ \dot{x}_4=-d_{xy}x_2-d_{yy}x_4-\omega_{xy}x_1-\omega_y^2x_3-2\Omega_zx_2 \\ \qquad +d_y+D\left(u_y\right) \end{array} \quad (2)$$

In Equation (2), a set of new parameters are introduced, such as:

$$\left.\begin{array}{c} d_{xx}=\frac{d_{xx}^*}{m\omega_0},d_{xy}=\frac{d_{xy}^*}{m\omega_0} \\ d_{yy}=\frac{d_{yy}^*}{m\omega_0},\Omega_z=\frac{\Omega_z^*}{m\omega_0},\omega_x^2=\frac{k_{xx}}{m\omega_0^2} \\ \omega_{xy}=\frac{k_{xy}}{m\omega_0^2},\omega_y^2=\frac{k_{yy}}{m\omega_0^2},u_x=\frac{u_x^*}{m\omega_0^2q_0},u_y=\frac{u_y^*}{m\omega_0^2q_0} \end{array}\right\} \quad (3)$$

where m, q_0 and ω_0^2 represent the quality of the mass, the reference length, and the square of the x-axes and y-axes resonance frequencies, respectively.

In practical engineering applications, friction and clearance of the internal components of the MEMS gyroscope cause asymmetrical dead-zone characteristics, which reduce control accuracy and system performance (Juan and Fei, 2013; Liu, Gao, Tong, and Li, 2015; Na, 2013).Therefore, it is necessary to establish an adaptive auxiliary signal to compensate the influence derived from the dead-zone input. The asymmetrical dead-zone inputs of the x-axes and y-axes can be defined as

$$\left.\begin{array}{c} h_{ri}\left(u_i-m_{ri}\right),\ u_i\geq m_{ri} \\ 0,-m_{li}<u_i<m_{ri},\ i=x,y, \\ h_{li}\left(u_i+m_{li}\right),\ u_i\leq m_{li} \end{array}\right\}=D\left(u_i\right) \quad (4)$$

where h_{rx} and $h_{lx}$are the right and left slopes of the x-axes; h_{ry} and $h_{ly}$are the right and left slopes of the y-axes; m_{rx} and m_{lx}represent the breakpoints of the x-axes; m_{ry} and m_{ly} represent the breakpoints of the y-axes; and h_{ri}, h_{li}, m_{ri} and m_{li}, $i = x, y$ are positive constants. The dead-zone inputs can be rewritten as

$$D\left(u_i\right)=h_iu_i+m_i,\quad i=x,y, \quad (5)$$

where

$$\left.\begin{array}{l} h_{rx},\ u_x\geq m_{rx} \\ 0,\ -m_{lx}<u_x<m_{rx} \\ h_{lx},\ u_x\leq m_{lx} \end{array}\right\}=h_x$$

and

$$\left.\begin{array}{l} -h_{rx}m_{rx},\ u_x\geq m_{rx} \\ 0,\ -m_{lx}<u_x<m_{rx} \\ h_{lx}m_{lx},\ u_x\leq m_{lx} \end{array}\right\}=m_x$$

are constants of the x-axes dead-zone input.

$$\left.\begin{array}{l} h_{ry},\ u_y\geq m_{ry} \\ 0,\ -m_{ly}<u_y<m_{ry} \\ h_{lx},\ u_y\leq m_{ly} \end{array}\right\}=h_y$$

and

$$\left.\begin{array}{l} -h_{ry}m_{ry},\ u_y\geq m_{ry} \\ 0,\ -m_{ly}<u_y<m_{ry} \\ h_{ly}m_{ly},\ u_y\leq m_{ly} \end{array}\right\}=m_y$$

are constants of the y-axes dead-zone input.

There is $\underline{h}_i = \min\left(h_{ri}, h_{li}\right) \leq |h_i| \leq \overline{h}_i = \max\left(h_{ri}, h_{li}\right)$, $|m_i| \leq \overline{m}_i = \max\left(h_{ri}m_{ri}, h_{li}m_{li}\right)$, $i = x, y$.

Remark 1: Zhang, Zhang, Liu, and Kim *et al.* proposed an adaptive control method based on neural networks for the asymmetric dead-zone input in nonlinear system (2009). However, it can only be applied to specific conditions without universality, such as

$$\left\{\begin{array}{l} x_i\left(k+1\right)=x_{i+1}\left(k\right), \quad i=1,\ldots,n-1 \\ x_n\left(k+1\right)=f\left(x\left(k\right)\right)+\Gamma\left(u\left(k\right)\right)+d_1\left(k\right), \end{array}\right.$$

and it has poor accuracy and robustness performance. The proposed scheme not only greatly reduces the chatter phenomenon, but also improves system performance and enhances its robustness to parameter uncertainty and external interference.

Dynamical analysis

In order to reveal the nonlinear characteristics of the MEMS gyroscope and explain the necessity of controller design, the dynamic analysis of the MEMS gyroscope is carried out when the dimensionless parameters of system are set as $\omega_x^2 = 355,3$, $\omega_y^2 = 532,9$, $\omega_{xy} = 70,99$, $d_{xx} = 0,01$, $d_{yy} = 0,01$, $\Omega_z = 0,1$ and $d_{xy} = 0,002$ (Rahmani and Rahman, 2019), and the initial values of the system states are set as $x_1(0) = 0,4$, $x_2(0) = 0$, $x_3(0) = 0,6$ and $x_4(0) = 0$. The sums of Lyapunov exponents x_1, x_2, x_3, and x_4 are $2,8884$, $-1,6952$, $1,1066$, and -3,501, respectively. The Kaplan-Yorke dimension of the MEMS gyroscope is calculated as $3,6569$ (Sambas, Mamat, Arafa, Mahmoud, and Sanjaya, 2019; Silva-Juarez, Rodriguez-Gomez, de la Fraga, Guillen-Fernandez, and Tlelo-Cuautle, 2019).

The phase diagrams and corresponding time histories are shown in Figure 2. The Lyapunov exponent diagram is shown in Figure 3. They reveal the dynamic characteristics of the MEMS gyroscope. It is easy to tell that the MEMS gyroscope exhibits chaotic motion. It is well known that this reduces accuracy and affects the running stability of the MEMS gyroscope. Meanwhile, this also fully illustrates thr fact that it is necessary to design a suitable control scheme to suppress the chaotic motion of the MEMS gyroscope and ensure the global asymptotic stability of the closed-loop system.

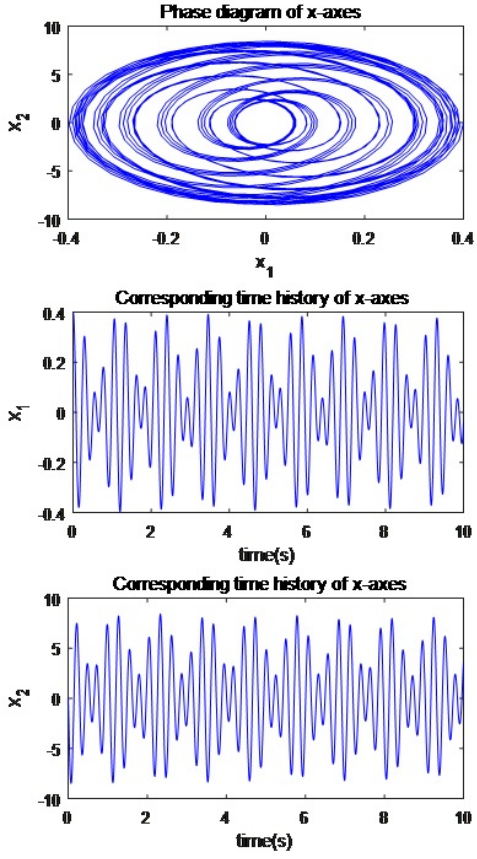

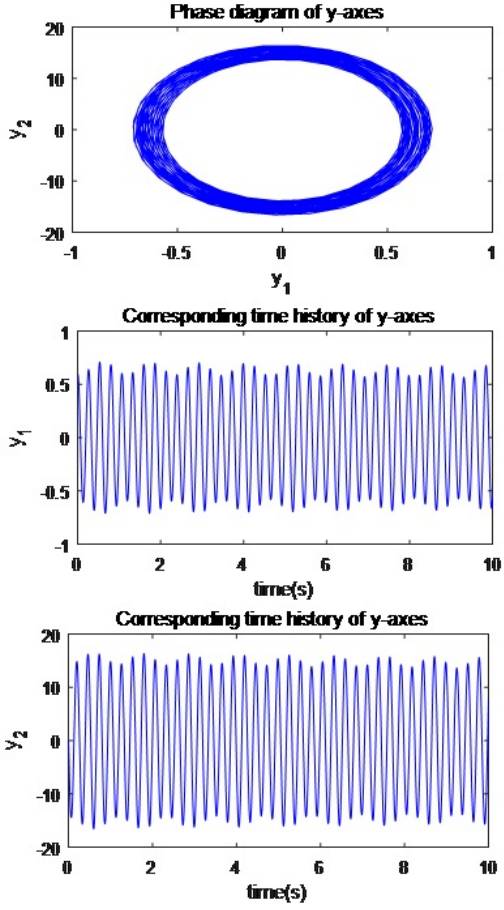

Figure 2. Phase diagrams and corresponding time histories.
Source: Authors

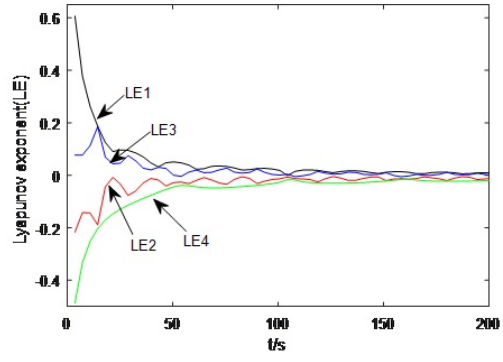

Figure 3. Lyapunov exponent diagram.
Source: Authors

Type-2 sequential fuzzy neural network

The T2SFNN is composed of fuzzy logic systems and neural networks. It avoids shortcomings such as slow speed, low precision, and high sample requirement of the fuzzy logic language and neural network reasoning (Mohammadzadeh and Ghaemi, 2018). The schematic diagram of the T2SFNN, consisting of the input layer, the fuzzification layer, the membership layer, the rule layer and the output layer, is

shown in Figure 4. The operating mechanism of the T2SFNN can be summarized as the following steps:

1) Based on the fuzzy theory, the upper input $\overline{I}_j^i$ and the lower input $\underline{I}_j^i$ on the membership layer can be written as

$$\left.\begin{aligned} \overline{I}_j^i &= \frac{\sigma_{\underline{A}_j}^2 c_{B_j^i} + \sigma_{\overline{B}_j^i}^2 I_j}{\sigma_{\underline{A}_j}^2 + \sigma_{\overline{B}_j^i}^2} \\ \underline{I}_j^i &= \frac{\sigma_{\underline{A}_j}^2 c_{B_j^i} + \sigma_{\underline{B}_j^i}^2 I_j}{\sigma_{\underline{A}_j}^2 + \sigma_{\underline{B}_j^i}^2}, \; j = 1,2,\ldots,n, \; i = 1,2,\ldots,l \end{aligned}\right\} \quad (6)$$

where $\sigma_{\overline{A}_j}^2$ and $\sigma_{\overline{B}_j^i}^2$ are the upper widths of the membership functions; $\sigma_{\underline{A}_j}^2$ and $\sigma_{\underline{B}_j^i}^2$ denote the lower widths of the membership functions; and $c_{B_j^i}$ and I_j represent the center and input of the membership function, respectively.

For Equation (6), the upper membership function and the lower membership function can be calculated as:

$$\overline{B}_j^i = \exp\left[\frac{-\left\|\overline{I}_j^i - c_{B_j^i}\right\|^2}{\sigma_{\overline{B}_j^i}^2}\right] \underline{B}_j^i = \exp\left[\frac{-\left\|\underline{I}_j^i - c_{B_j^i}\right\|^2}{\sigma_{\underline{B}_j^i}^2}\right] \quad (7)$$

2) A series of fuzzy IF-THEN rules set of the fuzzy neural network can be expressed in the following form:

IF I_1 is $B_1^i \cdots$ and I_j is B_j^i and $\cdots I_n$ is B_n^i, $j = 1,2,\ldots,n$, $i = 1,\ldots,l$, then

$$O \in \left[\overline{\theta}_i, \underline{\theta}_i\right], \quad (8)$$

whereB_j^i is the *ith* membership function for the *jth* input.

The upper and lower firing rules of the fuzzy neural network can be expressed in the following forms:

$$\left.\begin{aligned} \overline{\xi}_i(t) &= r\overline{\xi}_i(t-1) + \overline{B}_j^i \\ \underline{\xi}_i(t) &= r\underline{\xi}_i(t-1) + \underline{B}_j^i, \quad i = 1,2,\ldots,l \end{aligned}\right\} \quad (9)$$

where $\overline{\xi}_i(t)$ and $\underline{\xi}_i(t)$ are the upper and lower of the fuzzy neural network *ith* rule at previous sample time, respectively; $\overline{\xi}_i(t-1)$ and $\underline{\xi}_i(t-1)$ indicate the upper and lower mapping degrees of the*ith*rule at the last sample time; r is the design parameter; $\overline{B}_j^i$ and $\underline{B}_j^i$ are the upper/lower membership functions.

3) The output of the T2SFNN can be written as:

$$O(t) = \frac{\sum_{i=1}^{l} \overline{\theta}_i(t)\overline{\xi}_i(t) + \sum_{i=1}^{l} \underline{\theta}_i(t)\underline{\xi}_i(t)}{2} \quad (10)$$

where $\overline{\theta}_i$ and $\underline{\theta}_i$ are considered to be the upper and lower of inputs, and they can be designed in the following forms:

$$\left.\begin{aligned} \overline{\theta}_i &= \overline{\alpha}_i^0(t) + \overline{\alpha}_i^1(t) I_1(t) + \cdots + \overline{\alpha}_i^n(t) I_n(t) \\ \underline{\theta}_i &= \underline{\alpha}_i^0(t) + \underline{\alpha}_i^1(t) I_1(t) + \cdots + \underline{\alpha}_i^n(t) I_n(t), \; i = 1,2,\ldots,l \end{aligned}\right\} \quad (11)$$

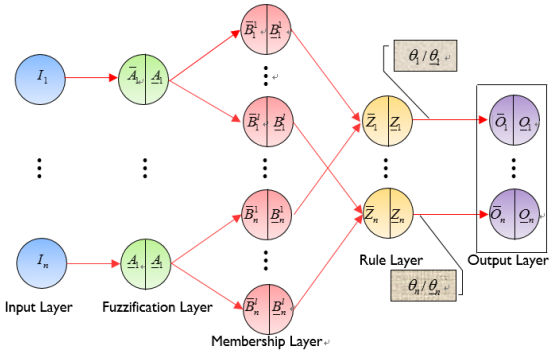

Figure 4. Schematic diagram of the T2SFNN.
Source: Authors

where $\overline{\alpha}_i^j(t), \underline{\alpha}_i^j(t)$, $i = 1,\ldots,l$, $j = 1,\ldots,n$ are the positive constant.

Equation (9) can be re-expressed as follows:

$$O(t) = \theta^T(t)\,\xi(t) \quad (12)$$

where

$$\theta(t) \equiv \begin{bmatrix} \overline{\alpha}_1^0,\ldots,\overline{\alpha}_1^n,\ldots,\overline{\alpha}_l^0,\ldots,\overline{\alpha}_l^n \\ \underline{\alpha}_1^0,\ldots,\underline{\alpha}_1^n,\ldots,\underline{\alpha}_l^0,\ldots,\underline{\alpha}_l^n \end{bmatrix}$$

is the weight vector,

$$\xi(t) = \begin{bmatrix} \overline{\xi}_1(t),\ldots,\overline{\xi}_1(t) I_n(t),\ldots,\overline{\xi}_l(t),\ldots,\overline{\xi}_l(t) I_n(t), \\ \underline{\xi}_1(t),\ldots,\underline{\xi}_1(t) I_n(t),\ldots,\underline{\xi}_l(t),\ldots,\underline{\xi}_l(t) I_n(t) \end{bmatrix}^T$$

is the input of the neural network.

Remark 2: With the increase of the membership layers, the approximation accuracy of the T2SFNN improves. However, calculation complexity increases significantly, which consumes too much computation time. Therefore, we adopt the golden section method to select the appropriate number of fuzzy layers. Then, the output accuracy meets the design requirements, and the computational complexity is acceptable.

Lemma 1 (Gao *et al.*, 2016): For any continuous function $f(x)$, there is a T2SFNN that satisfies

$$\sup_{x\in\Omega} \left|f(x) - \hat{f}(x,\theta)\right| \le \varepsilon(x), \quad (13)$$

where $\hat{f}$ is the estimation of f and $\varepsilon(x)$ is the approximate error of the T2SFNN.

We defined an optimal parameter θ^* being equal to $\arg\min_{\theta\in\Omega_\theta}\left[\sup_{x\in\Omega}\left|f(x) - \hat{f}(x,\theta)\right|\right]$, where Ω_θ is a compact set of x and Ω_θ is a compact set of θ. Let $\tilde{\theta} = \theta^* - \hat{\theta}$ with θ^* being a virtual item. For any constant $\overline{\varepsilon} > 0$, there is $|\varepsilon(x)| \le \overline{\varepsilon}$.

Controller design

The rate function to accelerate convergence is introduced as (Luo, Li, Li, and Hu, 2020):

$$\left.\begin{array}{cc} \frac{T^4\kappa(t)}{(1-b_\varphi)(T-t)^4+b_\varphi T^4\kappa(t)}, & 0\le t\le T \\ 1/b_\varphi, & t\ge T \end{array}\right\}=\varphi(t) \tag{14}$$

where $0<T<\infty$ is the specified time, $\kappa(t)$ represents any monotone non-decreasing time smoothing function satisfying $\kappa(0)=1$ and $\dot{\kappa}(t)\ge 0$. b_φ is a design parameter which satisfies $0<b_\varphi\ll 1$. Let $\beta_\varphi=\dot{\varphi}(t)/\varphi(t)$, where $\dot{\varphi}(t)$ is a continuous differentiable and bounded function. Additionally, $\varphi(t)$ is a positive and strictly monotone increasing function, and it has an initial value of $\varphi(0)=1$.

In order to avoid the explosion of differential complex terms associated with traditional backstepping, a second-order tracking differentiator is introduced (Tian *et al.*, 2014):

$$\left.\begin{array}{l} \dot{\vartheta}_1=-r_1\left|\vartheta_1-\alpha_r\right|^{1/2}sign\left(\vartheta_1-\alpha_r\right)+\vartheta_2 \\ \dot{\vartheta}_2=-r_2 sign\left(\vartheta_2-\dot{\vartheta}_1\right) \end{array}\right\} \tag{15}$$

where r_1, r_2 are positive numbers; α_r is the virtual control law; and ϑ_1 and ϑ_2 stand for the tracking differentiator states.

Lemma 2: If the initial condition$|\vartheta_1(t_0)-\alpha_r(t_0)|\le\wp$ with $\wp>0$, then, for any small positive numbersl_{ϑ_1} and l_{ϑ_2}, the following inequality holds:

$$|\vartheta_1-\alpha_r|\le l_{\vartheta_1}, |\vartheta_2-\dot{\alpha}_r|\le l_{\vartheta_2}. \tag{16}$$

Assumption 1: The desired tracking trajectories x_{id} and their derivatives are continuous and available, and they satisfy the constraints, so that$-t_i\le x_{id}\le t_i$, $i=1,3$.

Tracking errors are defined as

$$\left.\begin{array}{ll} e_i=x_i-x_{id}, & i=1,3 \\ e_i=x_i-\alpha_i, & i=2,4 \end{array}\right\} \tag{17}$$

where x_i, $i=1,\ldots,4$ are control inputs; α_i, $i=2,4$ stand for virtual control laws; and e_i, $i=1,\ldots,4$ indicate tracking errors.

At this time, the accelerated tracking compensation errors of the controller can be designed as follows:

$$S_i=\varphi e_i, \quad i=1,\ldots,4, \tag{18}$$

where S_i, $i=1,\ldots,4$ represent accelerated errors.

According to the idea of backstepping, the acceleration adaptive backstepping controller design includes four steps:

Step 1: The derivation of S_1 can be deduced:

$$\dot{S}_1=\varphi\left(\beta_\varphi e_1+e_2+\alpha_2-\dot{x}_{1d}\right). \tag{19}$$

Then the virtual control α_2 is designed as

$$\alpha_2=-\frac{k_1 e_1}{M_1\cos\left(\pi S_1/2B_1\right)}-\beta_\varphi e_1+\dot{x}_{1d}, \tag{20}$$

where $M_1=\frac{2+\pi S_1\tan(\pi S_1/2B_1)/2B_1}{\cos(\pi S_1/2B_1)}$; k_1 is a positive constant; and the parameter $B_1>0$ satisfies the constraint of the accelerated error as $|S_1|<B_1$.

The first Lyapunov candidate function can be designed

$$V_1=\frac{S_1^2}{\cos\left(\pi S_1/2B_1\right)}. \tag{21}$$

Substituting Equation (20) into (19), the derivation ofV_1can be deduced as

$$\dot{V}_1=-\frac{k_1 S_1^2}{\cos\left(\pi S_1/2B_1\right)}+M_1 S_1 S_2. \tag{22}$$

Step 2: The derivation of S_2 can be calculated as follows:

$$\dot{S}_2=\varphi\left(\beta_\varphi e_2+f_2(\cdot)+d_x+u_x-\dot{\alpha}_2\right), \tag{23}$$

where $f_2(\cdot)=-d_{xx}x_2-d_{xy}x_4-\omega_x^2 x_1-\omega_{xy}x_3+2\Omega_2 x_4$ stands for an unknown nonlinear term, since system parameters such as d_{xx}, d_{xy}, ω_x^2, ω_{xy}, Ω_z are uncertain. The T2SFNN has strong nonlinear mapping abilities and can approximate any unknown nonlinear term with high precision. Consequently, one has

$$f_2(\cdot)=\theta_2^T\xi_2+\varepsilon_2. \tag{24}$$

The second Lyapunov candidate function is designed as

$$V_2=V_1+\frac{S_2^2}{\cos\left(\pi S_2/2B_2\right)}. \tag{25}$$

From Equation (25), the derivation of V_2 can be deduced as

$$\dot{V}_2=\dot{V}_1+S_2\dot{S}_2 M_2. \tag{26}$$

where $M_2=\frac{2+\pi S_2/2B_2\tan(\pi S_2/2B_2)}{\cos(\pi S_2/2B_2)}$.

According to Lemma 2, the derivative of α_2 can be obtained through a second-order tracking differential:

$$\left.\begin{array}{l} \dot{\vartheta}_3=-r_3\left|\vartheta_3-\alpha_2\right|^{1/2}sign\left(\vartheta_3-\alpha_2\right)+\vartheta_4 \\ \dot{\vartheta}_4=-r_4 sign\left(\vartheta_4-\dot{\vartheta}_3\right) \end{array}\right\} \tag{27}$$

where the bound filtering error satisfies $|\vartheta_4-\dot{\alpha}_2|\le l_{\vartheta_4}$.

The control input with the corresponding adaptive law can be designed as

$$u_x=-\hat{\theta}_2^T\xi_2-\beta_\varphi e_2+\vartheta_4 \tag{28}$$

$$\dot{\hat{\theta}}_2=\gamma_2 S_2 M_2\xi_2-2\lambda_2\hat{\theta}_2, \tag{29}$$

where the design parameter k_2, γ_2 and λ_2 are positive constants, and the parameter $B_2>0$ satisfies the constraint of the accelerated error as $|S_2|<B_2$.

Substituting Equations (22), (23) and (28) into (26) yields

$$\begin{aligned} \dot{V}_2\le&-\sum_{i=1}^{2}\frac{k_i S_i^2}{\cos\left(\pi S_2/2B_2\right)}+\frac{M_2^2 d_x^2}{2} \\ &-\varphi^2 S_2^2+\varphi S_2 M_2\left(f_2(\cdot)-\hat{\theta}_2^T\xi_2\right)+S_2 M_2\varphi l_{\vartheta_4}. \end{aligned} \tag{30}$$

Step 3: The derivative of S_3 to time t can be calculated as

$$\dot{S}_3 = \varphi\left(\beta_\varphi e_3 + e_4 + \alpha_4 - \dot{x}_{3d}\right). \tag{31}$$

And the chosen virtual control input $\alpha_4$as

$$\alpha_4 = -\frac{k_3\bar{e}_3}{M_3\cos\left(\pi S_3/2B_3\right)} - \beta_\varphi e_3 + \dot{x}_{3d}, \tag{32}$$

where $M_3 = \frac{2+\frac{\pi}{2B_3}S_3\tan(\pi S_3/2B_3)}{\cos(\pi S_3/2B_3)}$, the design parameter k_3 is a positive constant, and the parameter $B_3 > 0$ satisfies the constraints of the accelerated error as $|S_3| < B_3$.

The third Lyapunov candidate function can be designed as follows:

$$V_3 = V_2 + \frac{S_3^2}{\cos\left(\pi S_3/2B_3\right)}. \tag{33}$$

The derivation of V_3 can be deduced as

$$\dot{V}_3 = \dot{V}_2 + S_3\dot{S}_3M_3. \tag{34}$$

Substituting α_4, $\dot{S}_3$ and $\dot{V}_2$ into $\dot{V}_3$ yields

$$\begin{aligned}\dot{V}_3 \le &-\sum_{i=1}^{3}\frac{k_iS_i^2}{\cos\left(\pi S_i/2B_i\right)} - \frac{\varphi^2S_2^2}{2} + \frac{M_2^2d_x^2}{2}\\ &+ M_3S_3S_4 + \varphi S_2M_2\left(f_2(\cdot) - \hat{\theta}_2^T\xi_2\right)\\ &+ S_2M_2\varphi l_{\vartheta_4}.\end{aligned} \tag{35}$$

Step 4: The last Lyapunov candidate function can be designed as

$$V_4 = V_3 + \frac{S_4^2}{\cos\left(\pi S_4/2B_4\right)}. \tag{36}$$

where the parameter $B_4 > 0$ satisfies the constraints of the accelerated error as $|S_4| < B_4$.

Calculating the derivative of S_4 with respect to time t results in

$$\dot{S}_4 = \varphi\left(\beta_\varphi e_4 + f_4(\cdot) + d_y + u_y - \dot{\alpha}_4\right), \tag{37}$$

where $f_4(\cdot) = -d_{xy}x_2 - d_{yy}x_4 - \omega_{xy}x_1 - \omega_y^2x_3 - 2\Omega_2x_2$ stands for an unknown continuous function. We can employ the T2SFNN to approximate it again as

$$f_4(\cdot) = \theta_4^T\xi_4 + \varepsilon_4. \tag{38}$$

As in step 2, the derivative of α_4 can be obtained through a second-order tracking differential:

$$\left.\begin{aligned}\dot{\vartheta}_5 &= -r_5\left|\vartheta_5 - \alpha_4\right|^{1/2}sign\left(\vartheta_5 - \alpha_4\right) + \vartheta_6\\ \dot{\vartheta}_6 &= -r_6sign\left(\vartheta_6 - \dot{\vartheta}_5\right)\end{aligned}\right\} \tag{39}$$

where the bound filtering error satisfies $|\vartheta_6 - \dot{\alpha}_4| \le l_{\vartheta_6}$.

The control input with the corresponding adaptive law can be designed as

$$u_y = -\hat{\theta}_4^T\xi_4 - \beta_\varphi e_4 + \vartheta_6 \tag{40}$$

$$\dot{\hat{\theta}}_4 = \gamma_4S_4M_4\xi_4 - 2\lambda_4\hat{\theta}_4, \tag{41}$$

where the design parameters k_4, γ_4 and λ_4 are positive.

The derivative of V_4 can be computed as follows:

$$\dot{V}_4 = \dot{V}_3 + S_4\dot{S}_4M_4 \tag{42}$$

where $M_4 = \frac{2+\frac{\pi}{2B_4}S_4\tan(\pi S_4/2B_4)}{\cos(\pi S_4/2B_4)}$.

Substituting u_y, $\dot{S}_4$ and $\dot{V}_3$ into $\dot{V}_4$ yields

$$\begin{aligned}\dot{V}_4 \le &-\sum_{i=1}^{4}\frac{k_iS_i^2}{\cos\left(\pi S_i/2B_i\right)}\\ &+\sum_{j=2,4,k=x,y}\frac{M_j^2d_k^2}{2} - \sum_{j=2,4}\varphi^2S_j^2/2\end{aligned} \tag{43}$$

Stability analysis

Lemma 3: Consider the control equation of the MEMS gyroscope described by Equation (2). The accelerated adaptive backstepping control inputs are designed as (20), (28), (32) and (40) with adaptive laws (29), (41). If Assumption 1 holds, and the initial conditions of the MEMS gyroscope with dead-zone inputs satisfy $x_1(0) \in (-B_1 + x_{1d}(0), B_1 + x_{1d}(0))$ and $x_3(0) \in (-B_3 + x_{3d}(0), B_3 + x_{3d}(0))$, then the following conclusions can be drawn:

1) All signals in the closed system are ultimately bounded in a uniform way, and the output constraint is never violated.

2) The issues with chaos oscillation and asymmetric dead-zone in the MEMS gyroscope system are solved, and the transient response speed of the system is improved by employing an acceleration function.

Proof: The whole Lyapunov function candidate is chosen as

$$V = \sum_{i=1}^{4}\frac{S_i^2}{\cos\left(\pi S_i/2B_i\right)} + \sum_{i=2,4}\frac{1}{2\gamma_i}\tilde{\theta}_i^T\tilde{\theta}_i. \tag{44}$$

The derivation of V regard to the time is

$$\dot{V} \le \sum_{j=2,4}\left(\tilde{\theta}_j^T\left(S_jM_j\xi_j - \frac{1}{\gamma_j}\dot{\hat{\theta}}_j\right) + \frac{M_j^2\varepsilon_j^2}{2}\right) \tag{45}$$

Substituting Equations (29) and (41) into (45) yields

$$\dot{V} \le \sum_{j=2,4}\left(\frac{\lambda_j}{\gamma_j}\left(2\theta_j^{*T}\hat{\theta}_j - 2\theta_j^T\hat{\theta}_j\right) + \frac{M_j^2\varepsilon_j^2}{2}\right) \tag{46}$$

From the Young's inequality, the following can be obtained:

$$\left.\begin{aligned}&\theta^{*T}\theta^* + \hat{\theta}^T\hat{\theta} \ge 2\theta^{*T}\hat{\theta}\\ &\theta^{*T}\hat{\theta} - \hat{\theta}^T\hat{\theta} \le \tfrac{1}{2}\theta^{*T}\theta^* - \tfrac{1}{2}\hat{\theta}^T\hat{\theta}\end{aligned}\right\} \tag{47}$$

Substituting (47) into (46) yields

$$\begin{aligned}\dot{V} \le &-\sum_{i=1}^{4}\frac{k_iS_i^2}{\cos\left(\pi S_i/2B_i\right)} + \sum_{j=2,4}\frac{M_j^2l_{\vartheta_{j+2}}^2}{2} + \sum_{j=2,4,k=x,y}\frac{M_j^2d_k^2}{2}\\ &+\sum_{i=2,4}\left(\frac{\lambda_j}{\gamma_j}\left(-\theta_j^{*T}\theta_j^* - \hat{\theta}_j^T\hat{\theta}_j\right) + \frac{2\lambda_j}{\gamma_j}\theta_j^{*T}\theta_j^{*T} + \frac{M_j^2\varepsilon_j^2}{2}\right).\end{aligned} \tag{48}$$

From $\tilde{\theta} = \theta^* - \hat{\theta}$, it has

$$\tilde{\theta}^T\tilde{\theta} = \theta^{*T}\theta^* - 2\theta^{*T}\hat{\theta} + \hat{\theta}^T\hat{\theta} \le 2\theta^{*T}\theta^* + 2\hat{\theta}^T\hat{\theta}. \tag{49}$$

From (48), Equation (47) can be rewritten as

$$\begin{aligned}\dot{V} \le & -\sum_{i=1}^{4}\frac{k_i S_i^2}{\cos(\pi S_i/2B_i)} + \sum_{j=,,4,k=x,y}\frac{M_j^2 d_k^2}{2} \\ & + \sum_{j=2,4}\left(\frac{2\lambda_j}{\gamma_j}\theta_j^{*T}\theta_j^* + \frac{M_j^2\varepsilon_j^2}{2} - \frac{\lambda_j}{2\gamma_j}\tilde{\theta}_j^T\tilde{\theta}_j\right) \\ & + \sum_{j=2,4}\frac{M_j^2 l_{\vartheta_{j+2}}^2}{2} = -a_0 V + b_0 + c_0.\end{aligned} \tag{50}$$

where $a_0 = \min\{k_1, k_2, k_3, k_4, \lambda_2, \lambda_4\}$, $b_0 = \sum_{j=2,4}\frac{M_j^2\varepsilon_j^2}{2} + \sum_{j=2,4}\frac{2\lambda_j}{\gamma_2}\theta_j^{*T}\theta_j^*$ and $c_0 = \sum_{j=2,4}\frac{M_j^2 l_{\vartheta_{j+2}}^2}{2} + \sum_{j=2,4,k=x,y}\frac{M_j^2 d_k^2}{2}$.

According to the general solution of the first-order linear differential equation, the solution of (50) can be expressed as

$$\dot{V}(t) \le \frac{b_0+c_0}{a_0} + \left(V(t_0) - \frac{b_0+c_0}{a_0}\right)e^{-a_0(t-t_0)} \tag{51}$$

thus defining a compact set as follows:

$$\Omega \equiv \{t \,|V(t) \le C_0\} \in \mathrm{R}. \tag{52}$$

where $C_0 = V(0) + \frac{b_0+c_0}{a_0}$.

From $\dot{V} \le -a_0 V + b_0 + c_0 < 0$, it can be obtained that all signals of the closed-loop system are ultimately bounded in a uniform way. There is

$$\left(S_1, S_2, S_3, S_4, \tilde{\theta}_2, \tilde{\theta}_4\right)^T \in \mathrm{R}^{6\times 1}. \tag{53}$$

By integrating Equation (50) into interval $[0, T]$, one has

$$\int_0^T \dot{V}dt \le -\int_0^T a_0\sum_{i=1}^{4}\frac{k_i S_i^2}{\cos(\pi S_i/2B_i)}dt + Tb_0 \tag{54}$$

After a series of mathematical transformations, (54) can be further expressed as

$$\begin{aligned}-\sum_{i=1}^{4}\int_0^T\frac{k_i S_i^2}{\cos(\pi S_i/2B_i)}dt \le & \frac{1}{a_0}(V(0) - V(T) + Tb_0) \\ & + \frac{1}{a_0}\int_0^T\left(\sum_{j=2,4}\frac{M_j^2 l_{\vartheta_{j+2}}^2}{2} + \sum_{j=2,4,k=x,y}\frac{M_j^2 d_k^2}{2}\right)dt.\end{aligned} \tag{55}$$

Since $-\frac{V(T)}{a_0} \le 0$, Equation (55) can be further expressed as follows

$$\begin{aligned}-\sum_{i=1}^{4}\int_0^T\frac{k_i S_i^2}{\cos(\pi S_i/2B_i)}dt \le & \frac{1}{a_0}(V(0) + Tb_0) \\ & + \int_0^T\left(\sum_{j=2,4}\frac{M_j^2 l_{\vartheta_{j+2}}^2}{2} + \sum_{j=2,4,k=x,y}\frac{M_j^2 d_k^2}{2}\right)dt.\end{aligned} \tag{56}$$

The convergence results show that the accuracy of the final error mainly depends on the upper bound of external disturbances and approximation errors.

Numerical simulation

In this section, the results of the numerical simulation analysis are provided to testify the effectiveness of our scheme. Suppose that the initial values of the MEMS gyroscope are chosen as $x_1(0) = 0,4$, $x_2(0) = 0$, $x_3(0) = 0,6$ and $x_4(0) = 0$, the tracking trajectories are set as $x_{1d} = 0,1\sin(4,17t + 1) + 0,1$, and $x_{3d} = 0,12\sin(5,11t + 1,2) + 0,12$. The external disturbances can be defined as $d_x = x_1\sin(t)$ and $d_y = x_3\sin(t)$. The parameters of the designed controller are set as $k_1 = 112$, $k_2 = 64$, $k_3 = 128$, $k_4 = 72$, $\gamma_2 = 2$, $\gamma_4 = 2$, $\lambda_2 = 1,5$, $\lambda_4 = 1,5$. Additionally, the center of membership functions are chosen as $[-1, -0,5, 0, 0,5, 1]$. The parameters of the T2SFNN are selected as $\sigma_{\overline{\mu}_j^i} = 1$, $\sigma_{\underline{\mu}_j^i} = 0,1$, $\sigma_{\overline{f}_j} = 0,5$, $\sigma_{\underline{f}_j} = 0,05$ and $r = 0,05$.

Trajectory tracking is shown in Figure 5. It is obvious that the desired tracking trajectories almost match the actual signal trajectories throughout the course of time, while it shows that the proposed scheme can suppress chaotic motion. Trajectory tracking errors of x-axis and y-axis for different external disturbances are depicted in Figure 6. For different external disturbances, tracking errors only have a small fluctuation in the beginning. This shows that the designed control scheme can eliminate the interference originated from external disturbances. Control inputs for different Ω_z are depicted in Figure 7. From it, we can determine that the control output is almost unaffected as parameter Ω_z changes. Obviously, the proposed control scheme has a strong robustness to parameter perturbations.

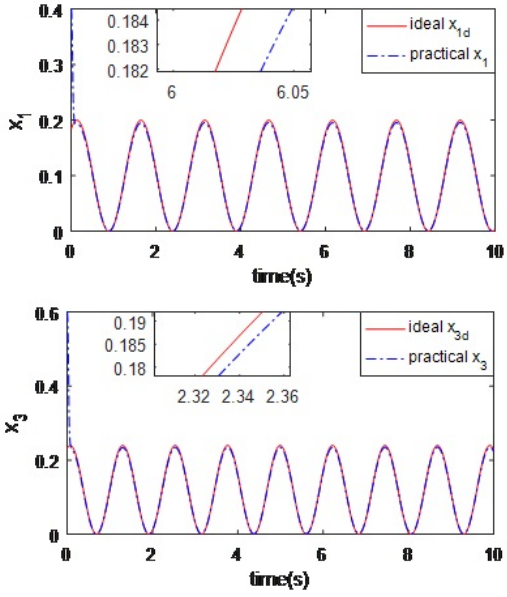

Figure 5. Position tracking of x-axis and y-axis.
Source: Authors

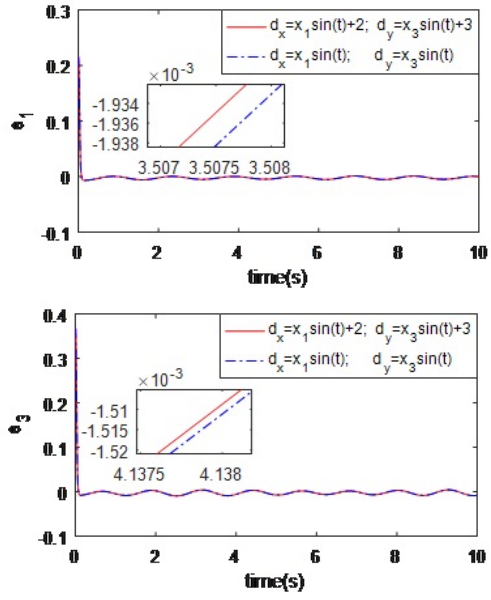

Figure 6. Position tracking errors of x-axis and y-axis for different external disturbances.
Source: Authors

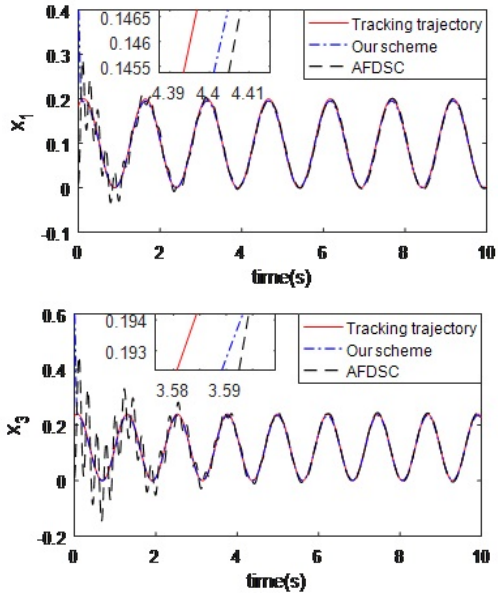

Figure 8. Position tracking contrast of x-axis and y-axis between adaptive fuzzy dynamic surface control and the proposed method.
Source: Authors

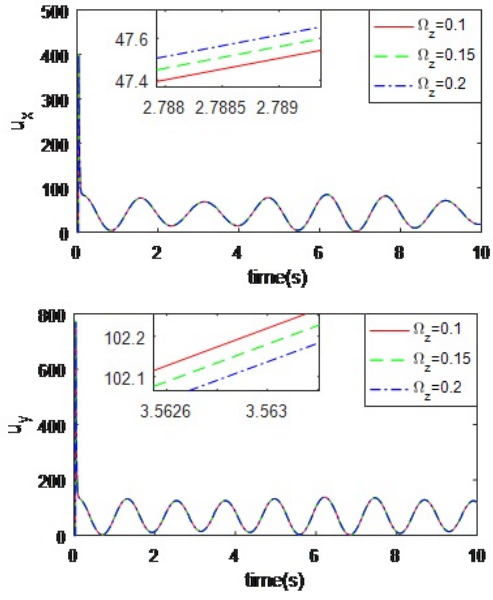

Figure 7. Control inputs of x-axis and y-axis for different Ω_z.
Source: Authors

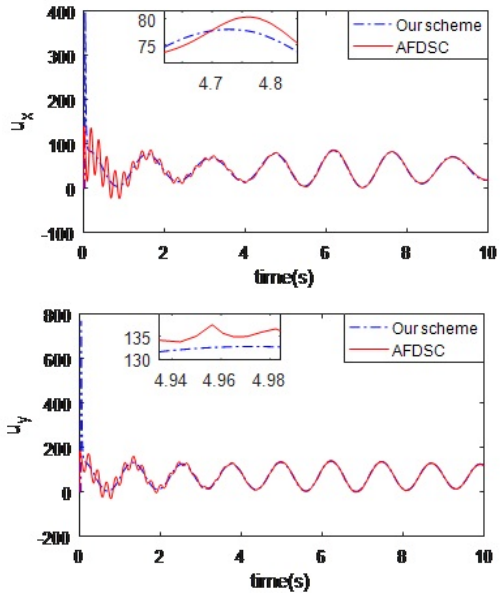

Figure 9. Control inputs contrast of x-axis and y-axis between adaptive fuzzy dynamic surface control and the proposed method.
Source: Authors

To show the superiority of our scheme, we made a comparison with adaptive fuzzy dynamic surface control (AFDSC) originated from (Lei, Cao, Wang, and Fei, 2017), and the control input can be written as follows:

$$u = -\hat{\theta}^T \xi(x) + \dot{\alpha}_1 - c_2 z_2 - \eta sgn(z_2), \qquad (57)$$

where $z_2 = x_2 - \alpha_1$, c_2 is a non-zone positive constant, the sliding mode term $\eta sgn(z_2)$ is a kind of compensation for the error of the fuzzy approximation, and η is a positive constant.

Figures 8 and 9 illustrate the trajectory tracking performance contrast between the adaptive fuzzy dynamic surface control and the proposed method. In turn, from Figures 7 and 8, it can be clearly concluded that the proposed control scheme has better performance than the adaptive fuzzy dynamic surface control.

Conclusion

In this paper, an accelerated adaptive backstepping control algorithm is proposed to address the control problem of the MEMS gyroscope with chaotic behavior, unknown external disturbances, and dead-zone inputs. In order to better reveal chaotic behavior of the MEMS gyroscope, the phase diagram and corresponding time history diagram are established. In the controller design process, the Lyapunov energy function is designed to make sure the output state of this system is constrained, the dead-zone control inputs are established to eliminate the adverse influence of the dead-zone input on the performance of the MEMS gyroscopes and T2SFNN is used to approximate unknown functions of the dynamic system. In order to accelerate the convergence speed and ensure that the system reaches a steady state faster, the speed function is established. The problem of complex terms explosion in traditional backstepping method is solved by combining the tracking differentiator with backstepping method. The stability analysis shows that the proposed scheme can ensure the global asymptotic stability of the closed-loop system. Finally, the simulation and comparison results show that the proposed control scheme has better control performance. In the near future, we will construct analog circuits to reveal the dynamic behavior of the fractional order MEMS gyroscope, and then design an effective controller to perform stable control of the fractional order MEMS gyroscope.

Acknowledgments

This project is supported by National Natural Science Foundation of China (Grant Nos. 52065008 and 61863005), Science and Technology Planning Project of Guizhou Province (Nos. [2020]1Y274, [2018]5781, [2019]2814, and [2020]6007) and Open Research Fund of Education Department of Guizhou Province (No.KYzhi[2019]041).

References

Chong, S., Rui, S., Jie, L., Xiaoming, Z., Jun, T., Yunbo, S., Jun, L., and Huiliang, C. (2016). Temperature drift modeling of MEMS gyroscope based on genetic-Elman neural network. *Mechanical Systems And Signal Processing, 72*, 897-905. 10.1016/j.ymssp.2015.11.004

Delavari, H., Lanusse, P., and Sabatier, J. (2013). Fractional order controller design for a flexible link manipulator robot. *Asian Journal of Control, 15*(3), 783-795. 10.1002/asjc.677

Fang, Y., Fei, J., and Yang, Y. (2018). Adaptive Backstepping Design of a Microgyroscope. *Micromachines, 9*(7), 338. 10.3390/mi9070338

Fang, Y., Yuan, Z., and Fei, J. (2015). Adaptive Fuzzy Backstepping Control of MEMS Gyroscope Using Dynamic Sliding Mode Approach. *Information Technology and Control, 44*(4), 380-386 10.5755/j01.itc.44.4.9110

Fei, J. and Chu, Y. (2016). Dynamic Global PID Sliding Mode Control for MEMS Gyroscope Using Adaptive Neural Controller. In IEEE (Eds.) 2016 Joint 8th International Conference on Soft Computing and Intelligent Systems (SCIS) and 17th International Symposium on Advanced Intelligent Systems (ISIS) (pp. 16-21). New York, NY: IEEE. 10.1109/SCIS-ISIS.2016.0018

Fei, J. and Zhou, J. (2012). Robust adaptive control of MEMS triaxial gyroscope using fuzzy compensator. *IEEE Transactions on Systems, Man, and Cybernetics, Part B* (*Cybernetics*), *42*(6), 1599-1607. 10.1109/TSMCB.2012.2196039

Gao, Ying, Tong, Shaocheng, Yongming, Liu, and Yan-Jun. (2016). Fuzzy Approximation-Based Adaptive Backstepping Optimal Control for a Class of Nonlinear Discrete-Time Systems With Dead-Zone. *IEEE Transactions on Fuzzy Systems: A Publication of the IEEE Neural Networks Council, 24*(1), 16-28. 10.1109/TFUZZ.2015.2418000

Gao, S., Dong, H., Ning, B., Tang, T., and Li, Y. (2018). Nonlinear mapping-based feedback technique of dynamic surface control for the chaotic PMSM using neural approximation and parameter identification. *IET Control Theory and Applications, 12*(6), 819-827. 10.1049/iet-cta.2017.0550

Juan, W. and Fei, J. (2013). Adaptive fuzzy approach for nonlinearity compensation in MEMS gyroscope. *Transactions of the Institute of Measurement and Control, 35*(8), 1008-1015. 10.1177/0142331212472224

Lei, D., Cao, D., Wang, T. and Fei, J. (2017). Adaptive Dynamic Surface Control of MEMS Gyroscope Sensor Using Fuzzy Compensator. *IEEE Access, 4*, 4148-4154. 10.1109/ACCESS.2016.2596538

Li, Z. and Kang, Y. (2010). Dynamic coupling switching control incorporating support vector machines for wheeled mobile manipulators with hybrid joints. *Automatica, 46*(5), 832-842. 10.1016/j.automatica.2010.02.019

Lin, J., Li, Y., and Yang, G. (2020). FPGAN: Face de-identification method with generative adversarial networks for social robots. *Neural Networks, 133*, 132-147. 10.1016/j.neunet.2020.09.001

Liu, Y.-J., Gao, Y., Tong, S., and Li, Y. (2015). Fuzzy approximation-based adaptive backstepping optimal control for a class of nonlinear discrete-time systems with dead-zone. *IEEE Transactions on Fuzzy Systems, 24*(1), 16-28. 10.1109/TFUZZ.2015.2418000

Luo, S., Li, J., Li, S., and Hu, J. (2020). Dynamical analysis of the fractional-order centrifugal flywheel governor system and its accelerated adaptive stabilization with the optimality. *International Journal of Electrical Power and Energy Systems, 118*, 105792. 10.1016/j.ijepes.2019.105792

Luo, S. and Song, Y. (2016). Chaos analysis-based adaptive backstepping control of the microelectromechanical resonators with constrained output and uncertain time delay. *IEEE Transactions on Industrial Electronics, 63*(10), 6217-6225. 10.1109/TIE.2016.2569462

Mohammadzadeh, A., and Ghaemi, S. (2018). Robust synchronization of uncertain fractional-order chaotic systems with time-varying delay. *Nonlinear Dynamics, 93*, 1809-1821. 10.1007/s11071-018-4290-2

Na, J. (2013). Adaptive prescribed performance control of nonlinear systems with unknown dead zone. *International Journal of Adaptive Control and Signal Processing, 27*(5), 426-446. 10.1002/acs.2322

Ouakad, H. M., Nayfeh, A. H., Choura, S., and Najar, F. (2015). Nonlinear feedback controller of a microbeam resonator. *Journal of Vibration and Control, 21*(9), 1680-1697. 10.1177/1077546313494112

Pan, Y., Wang, H., Li, X., and Yu, H. (2017). Adaptive command-filtered backstepping control of robot arms with compliant actuators. *IEEE Transactions on Control Systems Technology, 26*(3), 1149-1156. 10.1109/TCST.2017.2695600

Rahmani, M. (2018). MEMS gyroscope control using a novel compound robust control. *ISA transactions, 72*, 37-43. 10.1016/j.isatra.2017.11.009

Rahmani, M. and Rahman, M. H. (2018). A new adaptive fractional sliding mode control of a MEMS gyroscope. *Microsystem Technologies, 25*, 3409-3416.. 10.1007/s00542-018-4212-8

Rahmani, M. and Rahman, M. H. (2019). A novel compound fast fractional integral sliding mode control and adaptive PI control of a MEMS gyroscope. *Microsystem Technologies*, 1-7. 10.1007/s00542-018-4284-5

Sambas, A., Chang, H. L., Dolvis, L. G., Jacques, K., and Vaidyanathan, S. (2019). A new five-dimensional four-wing hyperchaotic system with hidden attractor, its electronic circuit realisation and synchronisation via integral sliding mode control. *International Journal of Modelling Identification and Control, 32*(1), 30-45. 10.1504/IJMIC.2019.10023534

Sambas, A., Mamat, M., Arafa, A. A., Mahmoud, G. M., and Sanjaya, W. S. M. (2019). A new chaotic system with line of equilibria: dynamics, passive control and circuit design. *International Journal of Electrical and Computer Engineering, 9*(4), 2365-2376. 10.11591/ijece.v9i4.pp2336-2345

Sambas, A., Vaidyanathan, S., Mamat, M., and Mohamed, M. A. (2020). Investigation of Chaos Behavior in a New Two-Scroll Chaotic System with Four Unstable Equilibrium Points, its Synchronization via Four Control Methods and Circuit Simulation. *IAENG International Journal of Applied Mathematics, 50*(1), 1-10. http://www.iaeng.org/IJAM/issues_v50/issue_1/IJAM_50_1_03.pdf

Silva-Juarez, A., Rodriguez-Gomez, G., de la Fraga, L. G., Guillen-Fernandez, O., and Tlelo-Cuautle, E. (2019). Optimizing the kaplan–yorke dimension of chaotic oscillators applying de and pso. *Technologies, 7*(2), 38. 10.3390/technologies7020038

Su, Z., Li, Y., and Yang, G. (2020). Dietary Composition Perception Algorithm Using Social Robot Audition for Mandarin Chinese. *IEEE Access*, (99), 8768-8782. 10.1109/ACCESS.2019.2963560

Sun, G. and Ma, Z. (2017). Practical tracking control of linear motor with adaptive fractional order terminal sliding mode control. *IEEE/ASME Transactions on Mechatronics, 22*(6), 2643-2653. 10.1109/TMECH.2017.2766279

Sun, T. and Pan, Y. (2019). Robust adaptive control for prescribed performance tracking of constrained uncertain nonlinear systems. *Journal of the Franklin Institute, 356*(1), 18-30. 10.1016/j.jfranklin.2018.09.005

Tian, D. P., Shen, H. H., and Dai, M. (2014). Improving the Rapidity of Nonlinear Tracking Differentiator via Feedforward. *IEEE Transactions on Industrial Electronics, 61*(7), 3736-3743. 10.1109/TIE.2013.2262754

Tong, S. and Li, Y. (2011). Adaptive fuzzy output feedback tracking backstepping control of strict-feedback nonlinear systems with unknown dead zones. *IEEE Transactions on Fuzzy Systems, 20*(1), 168-180. 10.1109/TFUZZ.2011.2171189

Vaidyanathan, S., Sambas, A., and Mamat, M. (2018). A new chaotic system with axe-shaped equilibrium, its circuit implementation and adaptive synchronization. *Archives of Control Sciences, 28*, 443-462. 10.24425/acs.2018.124711

Xiong, L., Wang, J., Mi, X., and Khan, M. W. (2017). Fractional order sliding mode based direct power control of grid-connected DFIG. *IEEE Transactions on Power Systems, 33*(3), 3087-3096. 10.1109/TPWRS.2017.2761815

Xu, B., Zhang, R., Li, S., He, W., and Shi, Z. (2019). Composite Neural Learning-Based Nonsingular Terminal Sliding Mode Control of MEMS Gyroscopes. *IEEE Transactions on Neural networks and learning systems, 31*(4), 1375-1386. 10.1109/TNNLS.2019.2919931

Yan, W., Hou, S., Fang, Y., and Fei, J. (2016). Robust adaptive nonsingular terminal sliding mode control of MEMS gyroscope using fuzzy-neural-network compensator. *International Journal of Machine Learning and Cybernetics, 8*, 1287-1299. 10.1007/s13042-016-0501-7

Hang, X., Zhang, H., Liu, D., and Kim, Y. (2009). Neural-network-based reinforcement learning controller for nonlinear systems with non-symmetric dead-zone inputs. Paper presented at the 2009 IEEE Symposium on Adaptive Dynamic Programming and Reinforcement Learning, 124-129. 10.1109/ADPRL.2009.4927535